ARTICLES
https://doi.org/10.1038/s41594-020-0441-5

nature structural & molecular biology

Check for updates

Cryo-EM structure of an amyloid fibril formed by full-length human prion protein

Li-Qiang Wang[1,6], Kun Zhao[2,3,6], Han-Ye Yuan[1], Qiang Wang[4], Zeyuan Guan[4], Jing Tao[1], Xiang-Ning Li[1], Yunpeng Sun[2,3], Chuan-Wei Yi[1], Jie Chen[1], Dan Li[5], Delin Zhang[4], Ping Yin[4], Cong Liu[2,7] ✉ and Yi Liang[1,7] ✉

Prion diseases are caused by the misfolding of prion protein (PrP). Misfolded PrP forms protease-resistant aggregates in vivo (PrP^{Sc}) that are able to template the conversion of the native form of the protein (PrP^{C}), a property shared by in vitro-produced PrP fibrils. Here we produced amyloid fibrils in vitro from recombinant, full-length human PrP^{C} (residues 23–231) and determined their structure using cryo-EM, building a model for the fibril core comprising residues 170–229. The PrP fibril consists of two protofibrils intertwined in a left-handed helix. Lys194 and Glu196 from opposing subunits form salt bridges, creating a hydrophilic cavity at the interface of the two protofibrils. By comparison with the structure of PrP^{C}, we propose that two α-helices in the C-terminal domain of PrP^{C} are converted into β-strands stabilized by a disulfide bond in the PrP fibril. Our data suggest that different PrP mutations may play distinct roles in modulating the conformational conversion.

Prions, meaning 'protein infectious agents', were initially described by S. B. Prusiner[1,2]. Prion disease is an infectious fatal neurodegenerative disease primarily caused by the misfolding of PrP proteins in humans, cattle, sheep and cervid species[1–9]. The conversion from the cellular native form, PrP^{C}, to the pathological aggregated form, PrP^{Sc}, is an important event in the initiation and progression of prion disease[1,2,6,8,10,11]. The structure of PrP^{C} features a largely disordered N-terminal tail and a folded C-terminal globular domain containing three α-helices and two short β-sheets[4,9,12]. In sharp contrast, PrP^{Sc} is predominantly composed of β-sheets[6,13–21], but atomic structural information is not available due to the insolubility and high heterogeneity of in vivo-derived material[7,10,13].

Substantial efforts have been dedicated to develop cell-free systems to generate PrP amyloid fibrils with physical properties that recapitulate those of PrP^{Sc} (refs. [22–24]). PrP fibrils produced in vitro have predominantly β-sheet structures and are proteinase K resistant, features similar to those of in vivo-derived PrP^{Sc} (refs. [22–25]). Transgenic mice overexpressing human PrP^{C} inoculated with in vitro-formed amyloid fibrils develop neurodegeneration characteristic of prion disease after long incubation times, suggesting their pathogenic potential[26–28]. Thus, determination of high-resolution structures of PrP fibrils should contribute to our understanding of prion disease.

Here we assemble homogeneous amyloid fibrils in vitro from recombinant, full-length human PrP^{C}, and determine their atomic structure using cryo-EM. While the infectivity of these fibrils remains to be established, the structural features provide insights into the conversion from α-helix-dominant PrP^{C} to β-sheet-rich PrP^{Sc}.

Results

Production of amyloid fibrils. We produced amyloid fibrils from recombinant, full-length human PrP^{C} (residues 23–231) expressed in *Escherichia coli*, by incubating the purified protein in 20 mM Tris-HCl buffer (pH 7.4) containing 2 M guanidine hydrochloride and shaking at 37 °C for 9–11 h (see Methods). PrP fibrils were dialyzed against NaAc buffer, purified by ultracentrifugation, resuspended in NaAc buffer and examined by electron microscopy without further treatment.

Negative-staining transmission electron microscopy (TEM) imaging showed that recombinant, full-length PrP^{C} formed homogeneous and unbranched fibrils (Fig. 1a). Congo red binding assays showed a red shift of the maximum absorbance, from 495 to 550 nm, in the presence of PrP fibrils (Extended Data Fig. 1a), which is typical of amyloid fibrils[29].

Proteinase K digestion of the PrP fibrils generated a predominant band with an apparent molecular weight of 15–16 kDa (Extended Data Fig. 1b). This is similar to a previously observed proteinase K-resistant fragment, also from human PrP fibrils assembled in vitro, shown by mass spectrometry to encompass residues 97–231 (refs. [24,25]). In addition, we also observed two other bands with apparent molecular weights of 12 and 10 kDa, respectively, after proteinase K digestion of the PrP fibrils (Extended Data Fig. 1b).

Structural characterization of PrP fibrils. We determined the atomic structure of PrP amyloid fibrils by cryo-EM (Table 1). The cryo-EM micrographs and two-dimensional (2D) class average images of the PrP fibrils show that each fibril is composed of two protofibrils intertwined in a left-handed helix (Extended Data Fig. 2a,b) and arranged in a staggered manner (Extended Data Fig. 2c). The fibrils are morphologically homogeneous, showing a fibril core diameter of ~14 nm and width of ~25 nm (Extended Data Fig. 2b). This is wider than previously described ex vivo, infectious PrP^{Sc} fibrils, which showed a width of ~20 nm (refs. [21,30]; based on negative staining on TEM) or ~10 nm (ref. [18]; based on cryo-EM images).

[1]Hubei Key Laboratory of Cell Homeostasis, College of Life Sciences, Wuhan University, Wuhan, China. [2]Interdisciplinary Research Center on Biology and Chemistry, Shanghai Institute of Organic Chemistry, Chinese Academy of Sciences, Shanghai, China. [3]University of Chinese Academy of Sciences, Beijing, China. [4]National Key Laboratory of Crop Genetic Improvement and National Center of Plant Gene Research, Huazhong Agricultural University, Wuhan, China. [5]Key Laboratory for the Genetics of Developmental and Neuropsychiatric Disorders, Ministry of Education, Bio-X Institutes, Shanghai Jiao Tong University, Shanghai, China. [6]These authors contributed equally: Li-Qiang Wang, Kun Zhao. [7]These authors jointly supervised this work: Cong Liu, Yi Liang. ✉e-mail: liulab@sioc.ac.cn; liangyi@whu.edu.cn

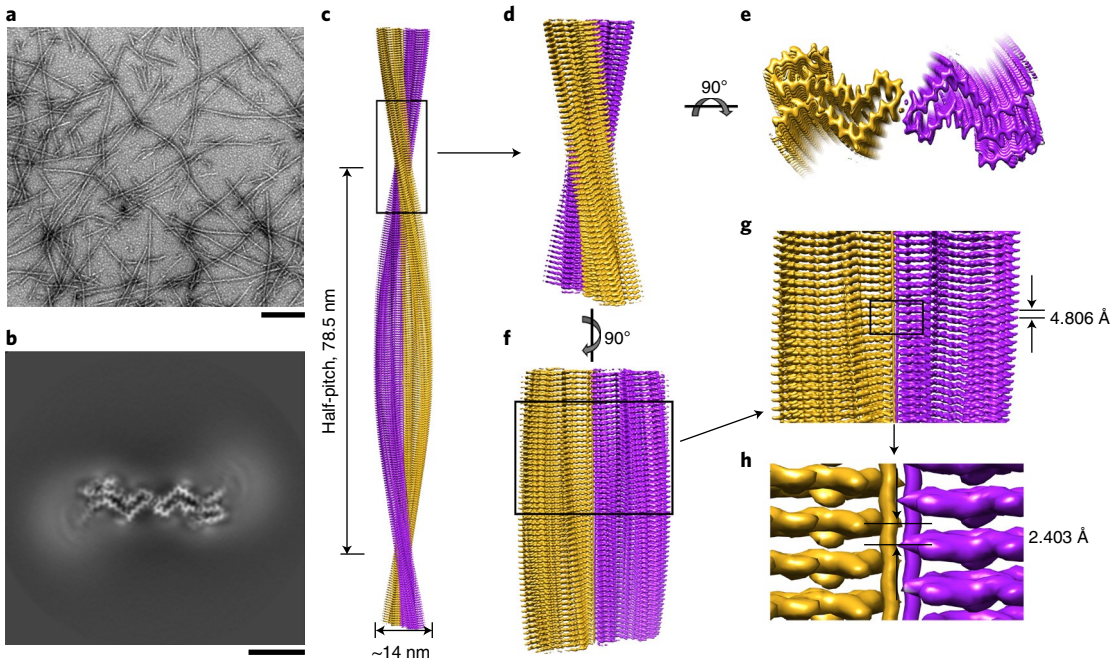

Fig. 1 | Cryo-EM structure of PrP fibrils. a, A negative-staining TEM image of amyloid fibrils from full-length human PrP. Scale bar, 500 nm. **b**, Cross-sectional view of the 3D map of these fibrils showing two protofibrils forming a dimer. Scale bar, 5 nm. **c**, 3D map showing two protofibrils intertwined in a left-handed helix, with a fibril core width of ~14 nm and a half-helical pitch of 78.5 nm. The two intertwined protofibrils are colored purple and gold, respectively. **d**, Enlarged section showing a side view of the density map. **e**, Top view of the density map. **f**, Another side view of the density map after 90° rotation of **d** along the fibril axis. **g**, Close-up view of the density map in **f** showing that the subunits in each protofibril stack along the fibril axis with a helical rise of 4.806 Å. **h**, Close-up view of the density map in **g** showing that the subunits in two protofibrils stack along the fibril axis with a helical rise of 2.403 Å.

This difference could be due to fibril polymorphism and/or fibril preparation procedures: for example, proteinase K digestion before cryo-EM imaging[18] would remove the flanking regions surrounding the fibril core.

Using helical reconstruction in RELION3.0 (ref. [31]), we determined a density map of the ordered core of PrP fibrils with an overall resolution of 2.70 Å and featuring well-resolved side chain densities and clearly separated β-strands along the helical axis (Fig. 1b and Extended Data Fig. 3a). The three-dimensional (3D) map showed two protofibrils intertwined in a left-handed helix, with a fibril core width of ~14 nm and a half-helical pitch of 78.5 nm (Fig. 1c). The protofilaments form a dimer with a screw symmetry of approximately 2_1 (Fig. 1d–f). The subunits in each protofibril stack along the fibril axis with a helical rise of 4.806 Å and twist of −1.102° (Fig. 1g), and the subunits in two protofibrils stack along the fibril axis with a helical rise of 2.403 Å (Fig. 1h).

We were able unambiguously to build the PrP fibril model comprising residues 170–229 (Fig. 2). Side chain densities for most residues had high local resolution (2.60–2.98 Å) (Extended Data Fig. 3b and Fig. 2a,b). The exterior of the fibril is mostly hydrophilic (Fig. 2b,g), whereas a hydrophobic core (Extended Data Fig. 4e), the intramolecular disulfide bond between Cys179 and Cys214 (Fig. 2a,b and Extended Data Fig. 4d) (also present in both PrP^C and PrP^{Sc} [13,17,18,20]) and a compact fold (Fig. 2b,d) help stabilize the fibril core, as described in detail below.

Six β-strand regions (β1–β6) are present in the structure observed in the PrP fibril core (Fig. 2b–d). The height of one layer, corresponding to one subunit, along the helical axis is 10.8 Å, which is the distance between the highest point in β3 and the lowest point in β6 (Fig. 2e). The protein backbone undergoes three right-angle turns: between β1 and β2 (at Cys179, which forms a disulfide bridge with Cys214); between β2 and β3; and between β3 and β4 at the dimer interface (Fig. 2b,d). All side chains of hydrophobic residues between β4 and β5 are located in the interior of the PrP fibril fold (Fig. 2b,d). A U-turn between β5 and β6 containing residues ^{217}QYERES^{222} (Extended Data Fig. 4f) enables the cross-β packing of those β-strands (Fig. 2b,d).

We identified three densities not connected to PrP in internal cavities formed by each protomer; these densities correspond to three ordered solvent molecules (Extended Data Fig. 5). In addition we found three other, unidentified, densities that are not connected to PrP in the cryo-EM map. Lys194 and Glu196 from opposing subunits form salt bridges that create a cavity at the interface of the two protofibrils (Figs. 1e and 2a,f,g and Extended Data Fig. 4a) containing two densities (Figs. 1e and 2a and Extended Data Figs. 3b and 4a). Furthermore, each monomer has an internal cavity containing extra density (Figs. 1e and 2a and Extended Data Figs. 3b and 4b). These three additional densities are strong but their identities are unclear: since the protein was purified from *E. coli* and fibrils were assembled in vitro, the densities probably correspond to contaminants but they are reminiscent of densities observed in the interior core of the protofilament in Tau fibrils from chronic traumatic encephalopathy brains[32], suggesting a broader role of cofactors in amyloid formation.

Previous work had shown that Asn181 and Asn197 are glycosylated in PrP^{Sc} (refs. [13,17,20]). The recombinant PrP we used is not glycosylated but, in our PrP fibril model, the side chains of those Asn residues appear well exposed to solvent (Fig. 2b and Extended Data Fig. 5) and should thus be able to accommodate bulky, N-linked glycans.

Discussion

We compared the structures of PrP^C and PrP fibrils (Fig. 3). Monomeric human PrP^C features a largely disordered N-terminal

Table 1 | Cryo-EM data collection, refinement and validation statistics

	PrP fibril (EMD-0931, PDB 6LNI)
Data collection and processing	
Magnification	29,000
Voltage (kV)	300
Camera	K2 summit
Frame exposure time (s)	0.2
Video frames (no.)	40
Electron exposure (e^-/Å^2)	64
Defocus range (μm)	−3.0 to −1.5
Pixel size (Å)	1.014
Symmetry imposed	*C*1
Box size (pixel)	400
Interbox distance (Å)	40.6
Micrographs collected (no.)	2,793
Segments extracted (no.)	381,747
Segments after Class 2D (no.)	285,958
Segments after Class 3D (no.)	86,012
Map resolution (Å)	2.704
FSC threshold	0.143
Map resolution range (Å)	2.6–4.5
Refinement	
Initial model used	De novo
Model resolution (Å)	2.7
FSC threshold	0.143
Model resolution range (Å)	2.7
Map sharpening *B* factor (Å^2)	-91.30
Model composition	
Nonhydrogen atoms	4,920
Protein residues	600
Ligands	0
B factors (Å^2)	
Protein	81.69
R.m.s. deviations	
Bond lengths (Å)	0.004
Bond angles (°)	0.540
Validation	
MolProbity score	2.16
Clashscore	10.67
Poor rotamers (%)	0
Ramachandran plot	
Favored (%)	87.41
Allowed (%)	12.59
Disallowed (%)	0

tail (residues 23–124) and a folded C-terminal globular domain containing three α-helices, two short β-sheets and a single disulfide bond between Cys179 in α2 and Cys214 in α3 (refs. [4,9,12]) (Fig. 3a,b). Thus, formation of the PrP fibril would require a major refolding of the C-terminal α-helical region of PrP^C, with α2 and α3 of PrP^C converted to β1, β2, β3, β5 and β6 and the loop between α2 and α3 converted to β4 in the PrP fibril (Fig. 3b,c).

Two alternative models of PrP^{Sc} based on low-resolution experimental data have been proposed. The parallel in-register intermolecular β-sheet model, based on spatial constraints from site-directed spin labeling and electron paramagnetic resonance studies[20] and on hydrogen/deuterium exchange analyses[19], predicts a major refolding of the C-terminal α-helical region of PrP^C, comprising residues ~160–220, into a mainly β-sheet conformation[19,20], which is in full agreement with our model. A β-solenoid model, based on low-resolution cryo-EM data using mouse anchorless PrP^{Sc} fibrils, predicts refolding of mouse PrP^C (89–230) into a four-rung β-sheet-rich conformation in which each rung has three β-strands[13,18]. This is partly compatible with our model, wherein β2, β3, β4 and β6 would correspond to the second and third β-strands in Rung 3 and the first and third β-strands in Rung 4 (ref. [13]); in both models, the fibril contains two intertwined protofibrils.

Among 42 mutations linked to genetic prion disease[1,3,5,9], 27 familial mutations are located within the PrP fibril core structure determined here (Fig. 3a). These mutations include those causing familial Creutzfeldt–Jakob disease (CJD), Gerstmann–Sträussler–Scheinker disease (GSS) and fatal familial insomnia (FFI)[1,3,5,9]. Notably, residues forming salt bridges (Lys194, Glu196 and Glu211) (Extended Data Fig. 4a,c) or hydrogen bonds (Gln217 and Tyr218) (Extended Data Fig. 4d,f) that contribute to maintenance of the PrP fibril structure are also prion disease-associated mutation sites. Those familial mutations, such as K194E, E196K, E211Q, E211D, Q217R and Y218N, would disrupt important interactions in PrP fibrils, suggesting that these variants would form PrP fibrils with structures distinct from the one presented here, which might be related to fibril polymorphism and mammalian prion strains[28].

Whether the fibril structure presented here is pathogenic remains to be established. Nevertheless, we hope that the structure will be valuable in regard to understanding the structural basis underlying PrP aggregation and inspire future research on the structural polymorphism of PrP fibrils and their relationship to prion diseases.

Online content

Any methods, additional references, Nature Research reporting summaries, source data, extended data, supplementary information, acknowledgements, peer review information; details of author contributions and competing interests; and statements of data and code availability are available at https://doi.org/10.1038/s41594-020-0441-5.

Received: 8 January 2020; Accepted: 28 April 2020;
Published online: 8 June 2020

References

1. Prusiner, S. B. Prions. *Proc. Natl Acad. Sci. USA* **95**, 13363–13383 (1998).
2. Prusiner, S. B. Molecular biology and pathogenesis of prion diseases. *Trends Biochem. Sci.* **21**, 482–487 (1996).
3. Scheckel, C. & Aguzzi, A. Prions, prionoids and protein misfolding disorders. *Nat. Rev. Genet.* **19**, 405–418 (2018).
4. Watts, J. C., Bourkas, M. E. C. & Arshad, H. The function of the cellular prion protein in health and disease. *Acta Neuropathol.* **135**, 159–178 (2018).
5. Kim, M.-O., Takada, L. T., Wong, K., Forner, S. A. & Geschwind, M. D. Genetic PrP prion diseases. *Cold Spring Harb. Perspect. Biol.* **10**, a033134 (2018).
6. Pan, K. M. et al. Conversion of α-helices into β-sheets features in the formation of the scrapie prion proteins. *Proc. Natl Acad. Sci. USA* **90**, 10962–10966 (1993).
7. Soto, C. Prion hypothesis: the end of the controversy? *Trends Biochem. Sci.* **36**, 151–158 (2011).

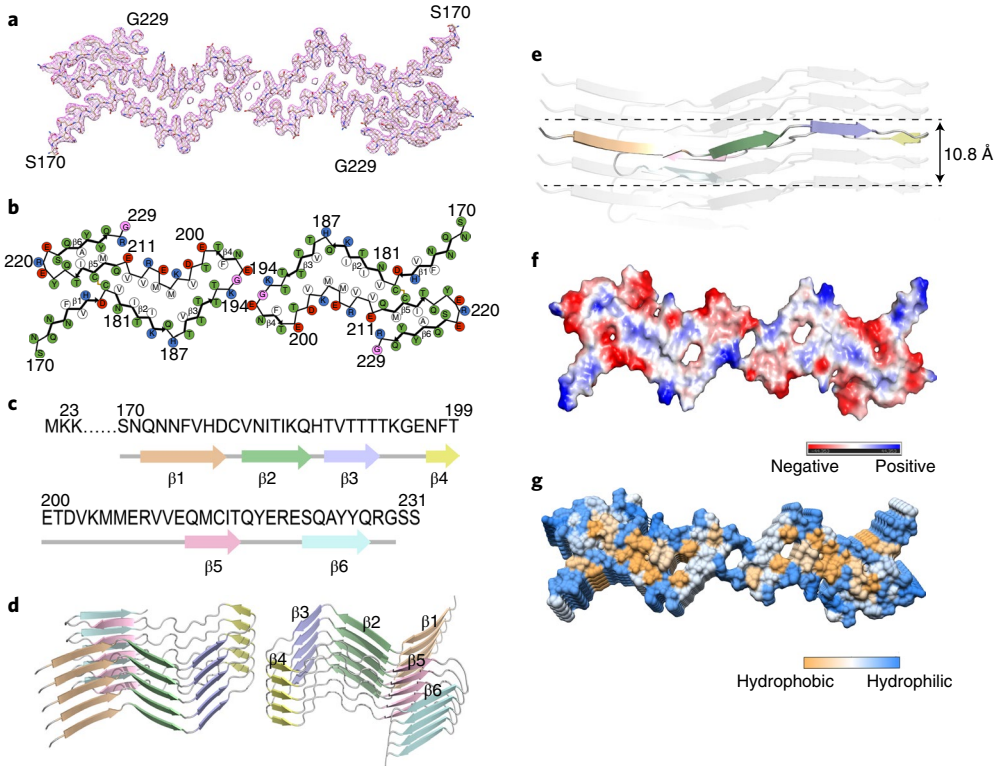

Fig. 2 | Atomic structure of PrP fibrils. a, Cryo-EM map of PrP fibrils with the atomic model overlaid. **b**, Schematic view of PrP fibril core. Residues are colored as follows: white, hydrophobic; green, polar; red and blue, negatively and positively charged, respectively; magenta, glycine. β-strands are indicated by bold lines. PrP fibrils are stabilized by a disulfide bond (yellow line) formed between Cys179 and Cys214 in each monomer, also visible in **a**. **c**, Sequence of the fibril core comprising residues 170–229 from full-length human PrP (23–231), with the observed six β-strands colored orange (β1), green (β2), blue (β3), yellow (β4), pink (β5) and cyan (β6). The dashed line corresponds to residues (23–169) not modeled in the cryo-EM density. **d**, Ribbon representation of the structure of a PrP fibril core containing five molecular layers and a dimer. **e**, As in **d**, but viewed perpendicular to the helical axis, revealing that the height of one layer of the subunit along the helical axis is 10.8 Å. **f**, Electrostatic surface representation of the structure of a PrP fibril core containing one molecular layer and a dimer. **g**, Hydrophobic surface representation of the structure of a PrP fibril core as in **d**. **f**,**g**, Lys194 and Glu196 from opposing subunits form salt bridges that create a cavity at the interface of the two protofibrils. The surface of two opposing subunits is shown according to the electrostatic properties (**f**) or the hydrophobicity (**g**) of the residues.

8. Prusiner, S. B. A unifying role for prions in neurodegenerative diseases. *Science* **336**, 1511–1513 (2012).
9. Rossetti, G., Cong, X., Caliandro, R., Legname, G. & Carloni, P. Common structural traits across pathogenic mutants of the human prion protein and their implications for familial prion diseases. *J. Mol. Biol.* **411**, 700–712 (2011).
10. Diaz-Espinoza, R. & Soto, C. High-resolution structure of infectious prion protein: the final frontier. *Nat. Struct. Mol. Biol.* **19**, 370–377 (2012).
11. Soto, C., Estrada, L. & Castilla, J. Amyloids, prions and the inherent infectious nature of misfolded protein aggregates. *Trends Biochem. Sci.* **31**, 150–155 (2006).
12. Zahn, R. et al. NMR solution structure of the human prion protein. *Proc. Natl Acad. Sci. USA* **97**, 145–150 (2000).
13. Spagnolli, G. et al. Full atomistic model of prion structure and conversion. *PLoS Pathog.* **15**, e1007864 (2019).
14. Wille, H. et al. Natural and synthetic prion structure from X-ray fiber diffraction. *Proc. Natl Acad. Sci. USA* **106**, 16990–16995 (2009).
15. Smirnovas, V. et al. Structural organization of brain-derived mammalian prions examined by hydrogen-deuterium exchange. *Nat. Struct. Mol. Biol.* **18**, 504–506 (2011).
16. Gallagher-Jones, M. et al. Sub-ångström cryo-EM structure of a prion protofibril reveals a polar clasp. *Nat. Struct. Mol. Biol.* **25**, 131–134 (2018).
17. Govaerts, C., Wille, H., Prusiner, S. B. & Cohen, F. E. Evidence for assembly of prions with left-handed β-helices into trimers. *Proc. Natl Acad. Sci. USA* **101**, 8342–8347 (2004).
18. Vázquez-Fernández, E. et al. The structural architecture of an infectious mammalian prion using electron cryomicroscopy. *PLoS Pathog.* **12**, e1005835 (2016).
19. Lu, X., Wintrode, P. L. & Surewicz, W. K. β-sheet core of human prion protein amyloid fibrils as determined by hydrogen/deuterium exchange. *Proc. Natl Acad. Sci. USA* **104**, 1510–1515 (2007).
20. Cobb, N. J., Sönnichsen, F. D., Mchaourab, H. & Surewicz, W. K. Molecular architecture of human prion protein amyloid: a parallel, in-register β-structure. *Proc. Natl Acad. Sci. USA* **104**, 18946–18951 (2007).
21. Terry, C. et al. Structural features distinguishing infectious *ex vivo* mammalian prions from non-infectious fibrillar assemblies generated *in vitro*. *Sci. Rep.* **9**, 376 (2019).
22. Bocharova, O. V., Breydo, L., Parfenov, A. S., Salnikov, V. V. & Baskakov, I. V. In vitro conversion of full-length mammalian prion protein produces amyloid form with physical properties of PrP^{Sc}. *J. Mol. Biol.* **346**, 645–659 (2005).
23. Tattum, M. H. et al. Elongated oligomers assemble into mammalian PrP amyloid fibrils. *J. Mol. Biol.* **357**, 975–985 (2006).
24. Zhou, Z. et al. Fibril formation of the rabbit/human/bovine prion proteins. *Biophys. J.* **101**, 1483–1492 (2011).
25. Pan, K., Yi, C. W., Chen, J. & Liang, Y. Zinc significantly changes the aggregation pathway and the conformation of aggregates of human prion protein. *Biochim. Biophys. Acta* **1854**, 907–918 (2015).
26. Legname, G. et al. Synthetic mammalian prions. *Science* **305**, 673–676 (2004).
27. Colby, D. W. et al. Protease-sensitive synthetic prions. *PLoS Pathog.* **6**, e1000736 (2010).
28. Colby, D. W. et al. Design and construction of diverse mammalian prion strains. *Proc. Natl Acad. Sci. USA* **106**, 20417–20422 (2009).
29. Yang, F. Jr., Zhang, M., Zhou, B. R., Chen, J. & Liang, Y. Oleic acid inhibits amyloid formation of the intermediate of α-lactalbumin at moderately acidic pH. *J. Mol. Biol.* **362**, 821–834 (2006).
30. Terry, C. et al. *Ex vivo* mammalian prions are formed of paired double helical prion protein fibrils. *Open Biol.* **6**, 160035 (2016).

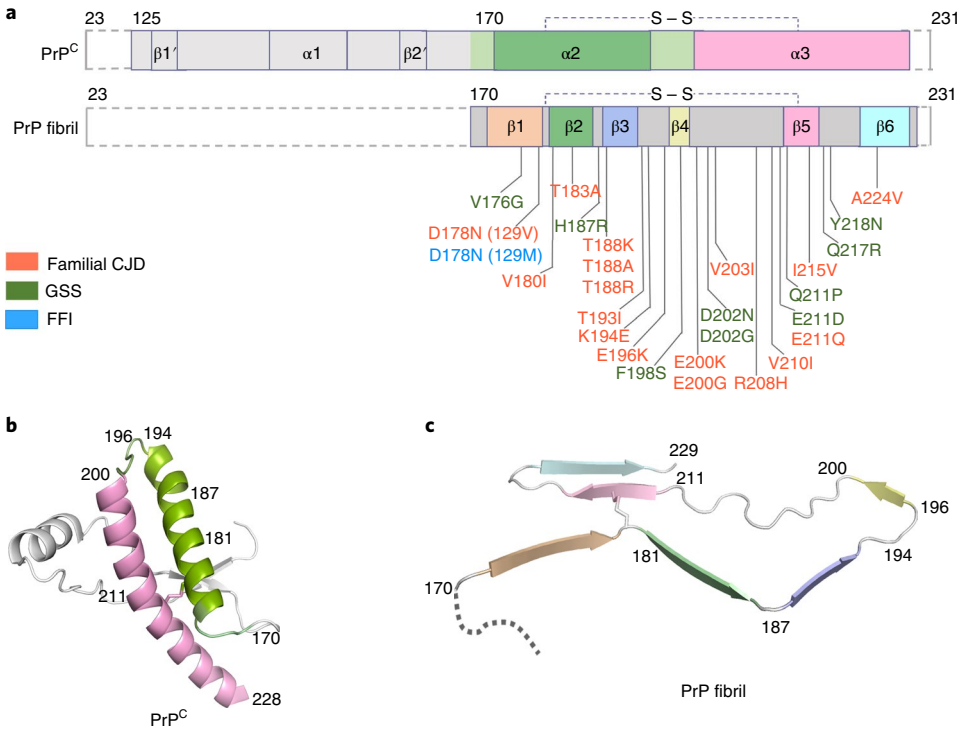

Fig. 3 | Comparison of the structures of PrP^C and PrP fibrils. a, Sequence alignment of the full-length human PrP^C (23–231) monomer with two short β-sheets, three α-helices and a single disulfide bond between Cys179 in α2 and Cys214 in α3 (PDB 1QLX)[12] and the PrP fibril core comprising residues 170–229 from full-length human PrP (23–231) with the observed six β-sheets and one disulfide bond between Cys179 in a loop (linking β1 to β2) and Cys214 in β5. S – S denotes a single disulfide bond. Twenty-seven familial mutations are located within the PrP fibril core structure. These mutations include those causing familial CJD, GSS and FFI[1,3,5,9]. **b**, Ribbon representation of the structure of the C-terminal domain (residues 125–228) of PrP^C with a disulfide bridge linking α2 and α3 (PDB 1QLX)[12]. **c**, Ribbon representation of the structure of a PrP fibril core containing one molecular layer and one subunit with a single disulfide bond. Dashed box (**a**) and dashed line (**c**) correspond to residues 23–169, which were not modeled in the cryo-EM density.

31. Zivanov, J. et al. New tools for automated high-resolution cryo-EM structure determination in RELION-3. *Elife* **7**, e42166 (2018).
32. Falcon, B. et al. Novel tau filament fold in chronic traumatic encephalopathy encloses hydrophobic molecules. *Nature* **568**, 420–423 (2019).

Methods

Protein purification. A plasmid-encoding, full-length human PrP (23–231) was a kind gift from G.-F. Xiao (Wuhan Institute of Virology, Chinese Academy of Sciences). PrP 23–231 was expressed from the vector pET-30a(+) in *E. coli* BL21 (DE3) cells (Novagen). PrP protein was purified by high-performance liquid chromatography on a C4 reverse-phase column (Shimadzu) as described by Bocharova et al.[33] and Zhou et al.[24]. After purification, recombinant PrP^C was dialyzed against 20 mM Tris-HCl buffer (pH 7.4) three times, concentrated, filtered and stored at −80 °C. SDS–PAGE and mass spectrometry were used to confirm that the purified human PrP was a single species with an intact disulfide bond. We used a NanoDrop OneC Microvolume UV-Vis Spectrophotometer (Thermo Scientific) to determine the concentration of human PrP^C, using its absorbance at 280 nm and the molar extinction coefficient calculated from the composition of the protein (http://web.expasy.org/protparam/).

PrP fibril formation. Full-length recombinant human PrP^C (120 μM) was incubated in 20 mM Tris-HCl buffer (pH 7.4) containing 2 M guanidine hydrochloride (GdnHCl) with shaking at 180 rpm at 37 °C for 9–11 h, and PrP fibrils were collected. Large aggregates in PrP fibril samples were removed by centrifugation at 5,000*g* at 4 °C for 10 min. The supernatant was then dialyzed against 20 mM NaAc buffer (pH 5.0) three times, to ensure that GdnHCl had been removed. After dialysis, PrP fibril samples were purified by ultracentrifugation at 100,000*g* for 30 min twice and washed with 20 mM NaAc buffer (pH 5.0). The pellet containing the fibrils was resuspended in 100 μl of 20 mM NaAc buffer (pH 5.0) and not treated with proteinase K. We used a NanoDrop OneC Microvolume UV-Vis Spectrophotometer (Thermo Scientific) to determine the concentration of PrP fibrils, using its absorbance at 280 nm and the molar extinction coefficient calculated from the composition of PrP (http://web.expasy.org/protparam/).

Congo red binding assays. Fibrils of full-length human PrP were analyzed by Congo red binding assays. A stock solution of 200 μM Congo red was prepared in PBS and filtered through a filter of 0.22 μm pore size before use. In a typical assay, the PrP fibril sample was mixed with a solution of Congo red to yield a final Congo red concentration of 65 μM and a final PrP concentration of ~13 μM, and the absorbance spectrum between 400 and 700 nm was then recorded on a UV-2550 Probe spectrophotometer (Shimadzu).

TEM of PrP fibrils. Amyloid fibrils of full-length human PrP were examined by electron microscopy of negatively stained samples. Ten microliters of PrP fibril samples (~13 μM) were loaded on copper grids for 30 s and washed with H_2O for 10 s. Samples on grids were then stained with 2% (w/v) uranyl acetate for 30 s and dried in air at 25 °C. The stained samples were examined using a JEM-1400 Plus transmission electron microscope (JEOL) operating at 100 kV.

Proteinase K digestion assay. Amyloid fibrils of full-length human PrP were assessed by proteinase K digestion. PrP fibril samples were incubated with proteinase K at a protease:PrP molar ratio of 1:100 to 1:50 for 1 h at 37 °C. Digestion was stopped by the addition of 2 mM phenylmethylsulfonyl fluoride, and samples were analyzed in 15% SDS–PAGE and detected by silver staining.

Cryo-EM of PrP fibrils. Amyloid fibrils of full-length human PrP were produced as described above. An aliquot of 3.5 μl of ~13 μM PrP fibril solution was applied to glow-discharged holey carbon grids (Quantifoil Au R1.2/1.3, 300 mesh), blotted for 6 s and plunge-frozen in liquid ethane using an FEI Vitrobot Mark IV. Grids were examined using an FEI Talos F200C microscope, operated at 200 kV and equipped with a field emission gun and a FEI Falcon III direct electron detector (Thermo Fisher). The cryo-EM micrographs were acquired on a FEI Titan Krios microscope operated at 300 kV (Thermo Fisher) and equipped with a Gatan K2 Summit camera. A total of 2,793 videos were collected in counting mode at a nominal magnification of ×29,000 (pixel size, 1.014 Å) and a dose of 8 e $Å^{-2}$ s^{-1} (see Table 1). An exposure time of 8 s was used, and the resulting videos were dose-fractionated into 40 frames. A defocus range of −1.5 to −3.0 μm was used.

Helical reconstruction. All 40 video frames were corrected for beam-induced sample motion and implemented dose weighting using MotionCor2 (ref. [34]). Contrast transfer function estimation of aligned, dose-weighted micrographs was performed by CTFFIND4.1.8 (ref. [35]). Subsequent image-processing steps, including manual picking, particle extraction, 2D classification, 3D classification, 3D refinement and post-processing, were performed using helical reconstruction methods in RELION3.0 (ref. [31]).

In total, 11,043 fibrils were picked manually from 2,793 micrographs, and 686 and 400 pixel boxes were used to extract particles by a 90% overlap scheme. Two-dimensional classification of 686-box-size particles was used to calculate the initial twist angle. In regard to helical rise, 4.8 Å was used as the initial value. Particles were extracted into 400-box sizes for farther processing. After several iterations of 2D and 3D classification, particles with the same morphology were picked out. Local searches of symmetry in 3D classification were used to determine the final twist angle and rise value. The 3D initial model was built by selected 2D classes; 3D classification was performed several times to generate a proper reference map for 3D refinement. Three-dimensional refinement of the selected 3D classes with appropriate reference was performed to obtain final reconstruction. The final map of PrP fibrils was convergent with a rise of 2.40 Å and twist angle of 179.45°. Post-processing was preformed to sharpen the map with a *B* factor of −88.36 $Å^2$. Based on the gold-standard Fourier shell correlation (FSC) = 0.143 criteria, the overall resolution was reported as 2.70 Å. The statistics of cryo-EM data collection and refinement are shown in Table 1.

Atomic model building and refinement. The map of PrP fibrils was sharpened using Phenix.auto_sharpen at the resolution cutoff indicated by map-map FSC[36]. COOT was used to build and modify the atomic model of PrP fibril without any reference model[37]. The model with five adjacent layers was generated for structure refinement. The model was refined using the real-space refinement program in PHENIX[38].

Reporting summary. Further information on experimental design is available in the Nature Research Reporting Summary linked to this article.

Data availability

Cryo-EM density maps and the atomic model of human PrP fibrils are available through the Electron Microscopy Data Bank and Protein Data Bank with accession codes EMD-0931 and PDB 6LNI, respectively. The Source Data for Extended Data Fig. 1 are available with the paper online.

References

33. Bocharova, O. V., Breydo, L., Salnikov, V. V. & Baskakov, I. V. Copper(II) inhibits in vitro conversion of prion protein into amyloid fibrils. *Biochemistry* **44**, 6776–6787 (2005).
34. Zheng, S. Q. et al. MotionCor2: anisotropic correction of beam-induced motion for improved cryo-electron microscopy. *Nat. Methods* **14**, 331–332 (2017).
35. Rohou, A. & Grigorieff, N. CTFFIND4: fast and accurate defocus estimation from electron micrographs. *J. Struct. Biol.* **192**, 216–221 (2015).
36. Terwilliger, T. C., Sobolev, O. V., Afonine, P. V. & Adams, P. D. Automated map sharpening by maximization of detail and connectivity. *Acta Crystallogr. D Struct. Biol.* **74**, 545–559 (2018).
37. Emsley, P., Lohkamp, B., Scott, W. G. & Cowtan, K. Features and development of Coot. *Acta Crystallogr. D Biol. Crystallogr.* **66**, 486–501 (2010).
38. Adams, P. D. et al. PHENIX: a comprehensive Python-based system for macromolecular structure solution. *Acta Crystallogr. D Biol. Crystallogr.* **66**, 213–221 (2010).

Acknowledgements

Y.L. and C.L. acknowledge funding from the National Natural Science Foundation of China (no. 31770833) and the Major State Basic Research Development Program (no. 2016YFA0501902). Y.L. also acknowledges financial support from the National Natural Science Foundation of China (nos. 31570779 and 31370774), the National Key Basic Research Foundation of China (no. 2013CB910702) and the Fundamental Research Fund for the Central Universities of China (no. 2015204020201). C.L. was also supported by the National Natural Science Foundation of China (no. 91853113), the Science and Technology Commission of Shanghai Municipality (no. 18JC1420500) and Shanghai Municipal Science and Technology Major Project (no. 2019SHZDZX02). P.Y. acknowledges financial support from the Major State Basic Research Development Program (no. 2018YFA0507700) and the National Natural Science Foundation of China (no. 31722017). Cryo-EM data were collected at the Center of Cryo Electron Microscopy, Zhejiang University, China. We thank G.-F. Xiao (Wuhan Institute of Virology, Chinese Academy of Sciences) for the kind gift of the human PrP^C plasmid; S. Chang (Center of Cryo Electron Microscopy, Zhejiang University) and X. Zhang (Zhejiang University School of Medicine) for their technical assistance with Cryo-EM; and Y. Wang (Institute of Biophysics, Chinese Academy of Sciences) for her helpful suggestions.

Author contributions

P.Y., C.L. and Y.L. supervised the project. L.-Q.W., P.Y., C.L. and Y.L. designed the experiments. L.-Q.W., H.-Y.Y., J.T., X.-N.L. and J.C. purified the PrP^C and PrP fibrils. L.-Q.W. and C.-W.Y. performed Congo red binding and proteinase K digestion assays of PrP fibrils. L.-Q.W., K.Z., H.-Y.Y., Q.W., Z.G., D.Z., Y.S. and D.L. collected, processed and/or analyzed cryo-EM data. L.-Q.W., K.Z., C.L. and Y.L. wrote the manuscript. All authors proofread and approved the manuscript.

Competing interests

The authors declare no competing interests.

Additional information

Extended data is available for this paper at https://doi.org/10.1038/s41594-020-0441-5.

Supplementary information is available for this paper at https://doi.org/10.1038/s41594-020-0441-5.

Correspondence and requests for materials should be addressed to C.L. or Y.L.

Peer review information Inês Chen was the primary editor on this article and managed its editorial process and peer review in collaboration with the rest of the editorial team.

Reprints and permissions information is available at www.nature.com/reprints.

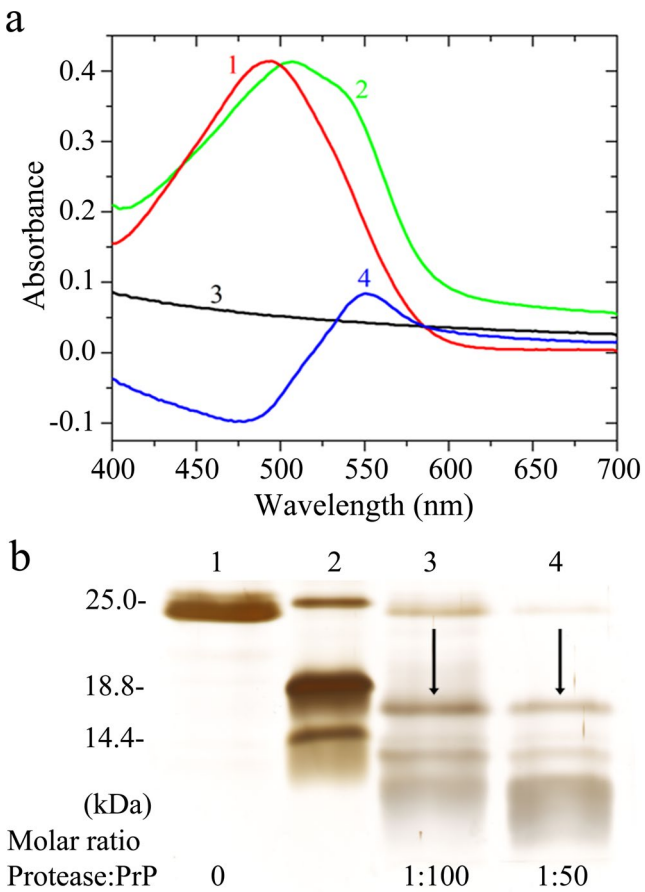

Extended Data Fig. 1 | PrP fibrils bind to Congo red and are proteinase K resistant. a, Amyloid fibrils of full-length human PrP analyzed by Congo red binding assays (**a**) or concentration-dependent proteinase K digestion assays (**b**)[24,25]. **a**, The difference spectra (Curve 4, blue) with the maximum absorbance at 550 nm were obtained by subtracting the absorbance spectra of PrP fibrils alone (Curve 3, black) and Congo red alone (Curve 1, red) with the maximum absorbance at 495 nm from those of PrP fibrils + Congo red (Curve 2, green). Congo red binding assays were carried out at 37 °C. **b**, Protease-resistant core fragment of 15–16-kDa is highlighted using a black arrow. Samples were treated with proteinase K for 1 h at 37 °C at protease:PrP molar ratios of 1:100 (lane 3) and 1:50 (lane 4). The control with no protease was loaded in lane 1. Molecular weight markers were loaded on lane 2: restriction endonuclease Bsp98 I (25.0 kDa), β-lactoglobulin (18.4 kDa), and lysozyme (14.4 kDa). Protein fragments were separated by SDS-PAGE and detected by silver staining. These experiments were repeated three times with different batches of fibrils and similar results. Data behind graph and uncropped images are available as source data.

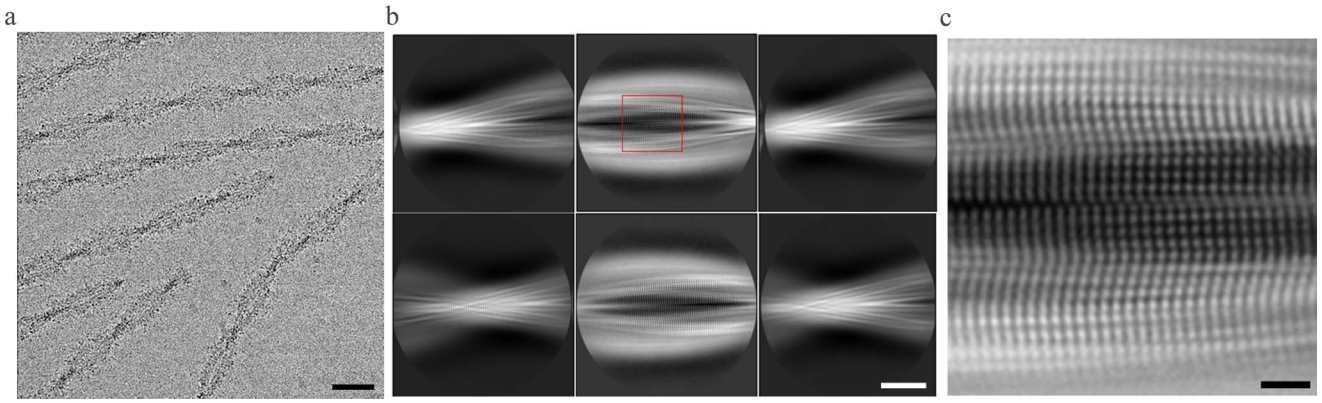

Extended Data Fig. 2 | Cryo-EM images of PrP fibrils. a, Cryo-EM micrographs of amyloid fibrils of full-length human PrP showing two protofibrils intertwined into a left-handed helix. Scale bar, 50 nm. **b**, Reference-free 2D class averages of PrP fibrils showing two protofibrils intertwined. Scale bar, 10 nm. **c**, Enlarged image of (**b**) showing two protofibrils arranged in a staggered manner. Scale bar, 2 nm.

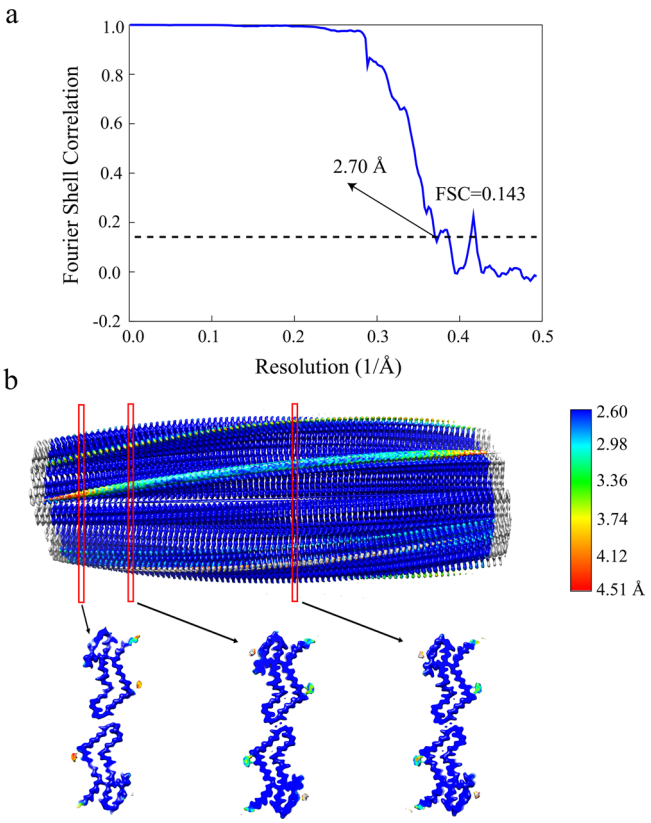

Extended Data Fig. 3 | Global (a) and local resolution (b) estimates for the PrP fibril reconstructions. a, Gold-standard refinement was used for estimation of the density map resolution. The global resolution of 2.70 Å was calculated using a Fourier shell correlation (FSC) curve cut-off at 0.143. **b**, The density map of PrP fibrils is colored according to local resolution estimated by ResMap. The three enlarged cross sections show the left top view of the density map of two protofibrils. The color key on the right shows the local structural resolution in angstroms (Å) and the colored map indicates the local resolution ranging from 2.6 to 4.5 Å.

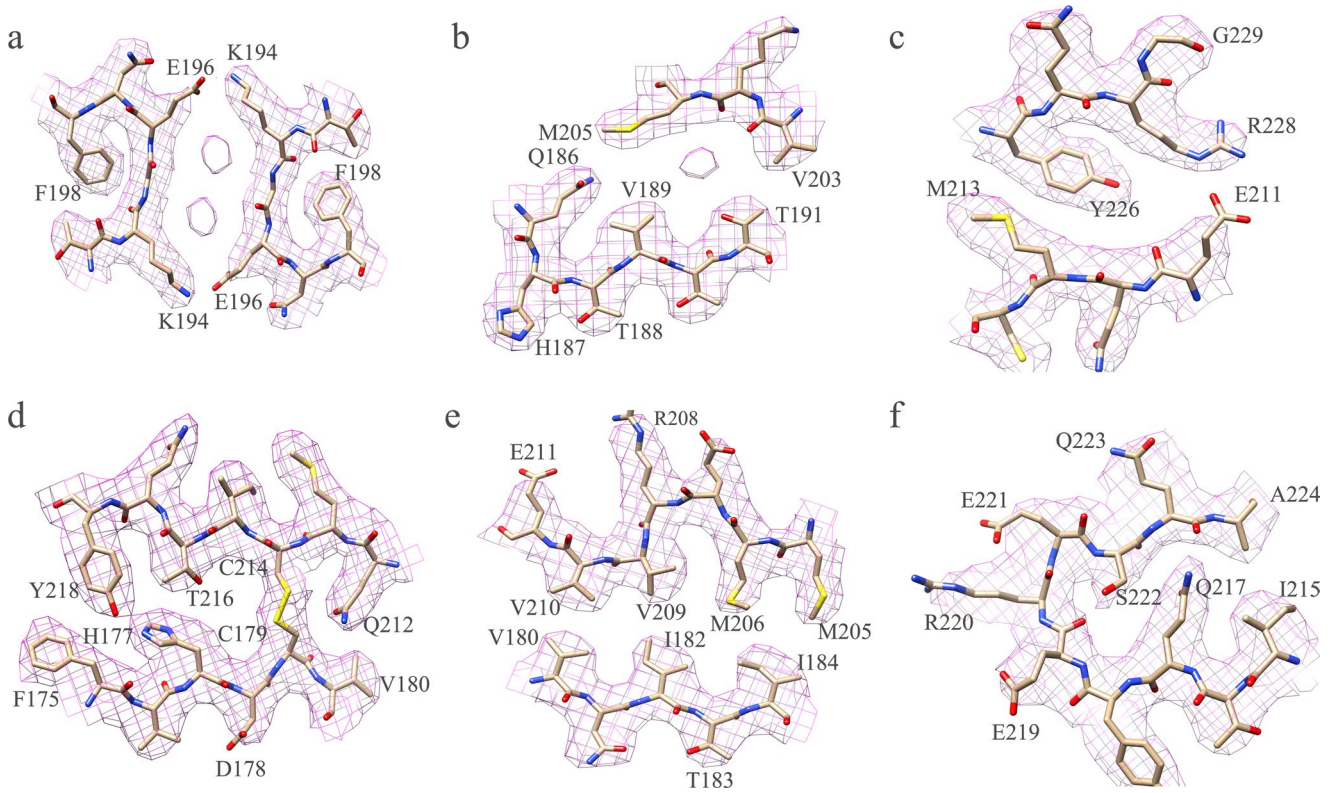

Extended Data Fig. 4 | Close-up view of the density map of PrP fibrils with the atomic model overlaid. a, The dimer interface comprises residues Lys194, Gly195, and Glu196 from both subunits. Two salt bonds are formed between Lys194 and Glu196 from opposing subunits to create a hydrophilic cavity at the dimerization interface. **b**, An inner cavity in each subunit formed by Gln186, Val189, and Thr191 on one side and Val203 and Met205 on the opposing side. **c**, A salt bridge is formed between Glu211 and Arg228. **d**, PrP fibrils are stabilized by one disulfide bond between Cys179 and Cys214. A hydrogen bond is formed between His177 and Tyr218. **e**, Hydrophobic side chains of Val180, Ile182, Ile184, Met205, Met206, Val209, and Val210 are located in the interior of PrP fibrils to form a stable hydrophobic core. **f**, A U-turn between β5 and β6 containing residues ^{217}QYERES^{222}. Three hydrogen bonds are formed between Gln217 and the main chain of Gln223, between Ser222 and the main chain of Glu219, and between Ser222 and the main chain of Arg220.

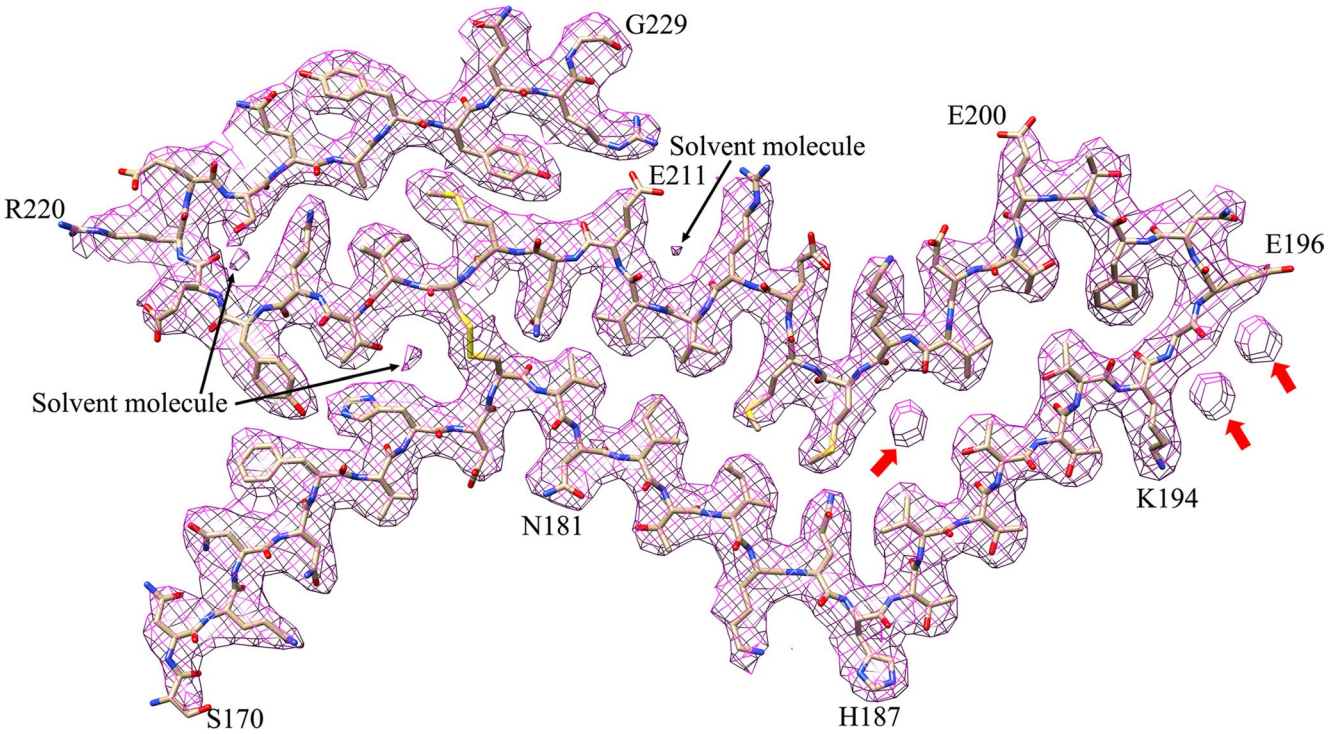

Extended Data Fig. 5 | Cryo-EM density map of human PrP fibril with the atomic model overlaid. A cavity at the interface of two protofibrils encloses two additional densities that are not connected to PrP. An internal cavity encloses extra density that is also not connected to PrP. Three ordered solvent molecules are found in the inner cavities.